Overhaul of the stratospheric lidar at Dumont d'Urville, Antarctica: three-wavelength setup, processing and observations

Florent Tencé[1], Julien Jumelet[1], Rafik Hassen-Khodja[2], Sophie Bounissou[2], Jean-François Mariscal[2], and Ismaël Charlet[3]

[1]LATMOS/IPSL, Sorbonne Université, UVSQ, CNRS, Paris, France
[2]LATMOS/IPSL, UVSQ Université Paris-Saclay, Sorbonne Université, CNRS, Guyancourt, France
[3]IPEV, Institut Paul-Émile Victor, Plouzané, France

Correspondence: Florent Tencé (florent.tence@latmos.ipsl.fr)

Abstract.

The stratospheric cloud and aerosol lidar instrument Liraan (*LIdar pour la Recherche Antarctique Aérosol et Nuages*) has been operated at the French Antarctic station Dumont d'Urville since 1989. Following a major upgrade conducted between 2022 and 2024, this paper presents the instrument configuration and its scientific capabilities. Liraan now enables the retrieval of backscatter coefficients at 355 nm, 532 nm and 1064 nm and depolarization ratios at 355 nm and 532 nm. The new configuration is described in detail, along with an improved data inversion algorithm, which is further used as input to a dedicated microphysical retrieval methodology. A unified 532 nm lidar time series spanning 1991 - 2025 at Dumont d'Urville is also presented for the first time. Finally, 2025 multispectral lidar measurements are used in a case study of volcanic aerosol size distribution retrieval.

1 Introduction

Monitoring the southern polar stratosphere has been an active area of research over the last 50 years, particularly since the identification of the ozone hole in the 1970s and 1980s (Farman et al., 1985). Understanding the mechanisms governing stratospheric ozone chemistry rapidly became a major scientific priority and brought increased attention to stratospheric processes. In parallel, the development of spaceborne instruments has led to important scientific breakthroughs, particularly in regions with scarce instrumental coverage such as the polar middle and upper atmosphere.

Following the discovery of the ozone hole, Polar Stratospheric Clouds (PSC) were quickly identified as crucial microphysical precursors to the ozone chemistry (McCormick and Trepte, 1986; Poole and McCormick, 1988; Solomon, 1999). Soon after the Montreal Protocol, a stratospheric aerosol and cloud lidar was installed at the French Antarctic station Dumont d'Urville (DDU - 66°40 S, 140° E) in 1989. It was among the first stratospheric lidars deployed in Antarctica, after those at Syowa (Iwasaka et al., 1985; Iwasaka, 1986) and Amundsen-Scott stations (Fiocco et al., 1992). Similar systems have since been installed in McMurdo, Rothera and Davis stations (Adriani et al., 1992, 2004; Innis and Klekociuk, 2006; Simpson et al., 2005). **McMurdo lidar was then relocated in Dome C, Concordia station in 2014 where it is still operated today (Snels et al., 2019, 2021; Cairo et al., 2023).** The DDU lidar provides the longest continuous measurement record of this type in

Antarctica and has contributed to stratospheric studies for several decades (Stefanutti et al., 1991, 1995; Bergeret et al., 1998; David-Beausire et al., 1998; David et al., 2005, 2010, 2012; Godin et al., 2001; Santacesaria et al., 2001; Guzzi et al., 1999; Jumelet et al., 2009, 2020; Sepúlveda et al., 2021; Tencé et al., 2022; Tencé et al., 2023).

Over the past three decades, knowledge of PSCs has considerably improved, largely driven by the advent of spaceborne observations: CALIOP aboard CALIPSO has provided an unprecedented global, vertically resolved three-dimensional view of PSC occurrence, composition, and seasonal variability (Pitts et al., 2009, 2011, 2013, 2018). Scientific efforts to understand PSC microphysical types, formation pathways, and interannual variability are synthesized in Tritscher et al. (2021) and have helped to better constrain chemical–microphysical interactions and improve the representation of PSC processes in chemistry–climate models. At DDU, a climatology based on 2007-2020 lidar measurements, compared with CALIOP observations, has contributed to these studies (Tencé et al., 2023). Despite significant progress in understanding PSC-related mechanisms, important questions remain regarding the stratospheric aerosols on which they strongly depend. Significant uncertainties persist concerning the abundance, composition, and radiative–chemical impacts of stratospheric aerosols. The comprehensive review by Kremser et al. (2016) highlighted the remaining gaps in our understanding of background aerosol variability and its response to natural and anthropogenic perturbations. More recent in situ observations have reported unexpectedly high fractions of carbonaceous aerosols in the lower stratosphere, challenging the traditional view of the Junge aerosol layer (Katich et al., 2023; Martinsson et al., 2019). Such findings raise important questions regarding aerosol composition of stratospheric aerosols, particularly their potential influence on heterogeneous chemistry and PSC formation, with implications for the expected recovery of the ozone layer.

In recent years, new challenges have emerged concerning the consequences of stratospheric perturbations. Stratospheric cloud fields are strongly influenced by variations in aerosol loading, whether driven by volcanism or by the transport of biomass burning aerosols from mid-latitudes. A notable example is the 2020 Australian wildfires (Solomon et al., 2022), whose aerosols penetrated the polar vortex and have been extensively studied. These events were well captured by lidar observations at DDU, where a layer of carbonaceous aerosols persisted in the stratosphere for nearly two years (Tencé et al., 2022). These aerosols disrupted stratospheric cloud fields, contributed to ozone anomalies, and raised key questions regarding their long-term sedimentation and the limits of current observational capabilities in discriminating between sulfate (volcanic) and carbonaceous (biomass-burning) particles. A multispectral lidar with depolarization capability is a particularly well-suited ground-based instrument to address these questions. The 2022 Hunga eruption further highlighted the diversity of stratospheric perturbations, with unprecedented injections of water vapor and aerosols in the upper stratosphere (Khaykin et al., 2022; Millán et al., 2022; Kloss et al., 2022). These events underscore the importance of monitoring episodic aerosol injections, together with dedicated modelling efforts to assess their chemical and radiative impacts in a changing climate.

Recent assessments of ozone recovery indicate a gradual return toward pre-1980 levels, consistent with the effectiveness of the Montreal Protocol (WMO, 2022). Updated projections suggest that Antarctic springtime ozone concentrations are expected to return to 1980 levels by the middle of the 21st century, although substantial interannual variability remains, and uncertainties persist regarding the vertical structure of recovery and a potential slowdown due to chemistry climate interactions (WMO, 2022). Dynamic variability, including sudden stratospheric warming events, volcanic perturbations, and wildfiretriggered aerosol injections continue to modulate ozone depletion processes through their impacts on temperature and chemical composition in both the gas and condensed phases. This highlights the need for sustained monitoring of ozone and stratospheric processes through aerosol and clouds observations.

In this context, and after the success of the 2006 - 2023 CALIPSO mission boarding the 532 nm CALIOP lidar (Winker et al., 2009), the EarthCARE mission was launched in 2024, carrying four instruments: a cloud profiling radar, a multispectral imager, a broadband radiometer and an atmospheric lidar (ATLID). ATLID is a high spectral resolution lidar (HSRL) operating at 355 nm and including a polarization channel. Its HSRL capability enables direct separation of Mie and Rayleigh scattering and provides high-quality measurements for a spaceborne lidar. The combination of high sensitivity, depolarization capability, and direct retrieval of the lidar ratio makes ATLID an optimal tool for the study of fine stratospheric aerosols. The wide range of available lidar products is described in Donovan et al. (2024); van Zadelhoff et al. (2023). The first studies exploiting ATLID stratospheric measurements are now emerging (Khaykin et al., 2026, e.g.,) and demonstrate very good performance. ATLID can be considered a successor to and an improvement over CALIOP, offering promising perspectives for the coming decade. The synergy between EarthCARE observations and ground-based measurements at DDU opens new opportunities for constraining stratospheric aerosol properties, PSC microphysics, and their role in polar ozone chemistry.

Maintaining the long-term scientific relevance of the DDU lidar requires regular maintenance and periodic instrumental upgrades. Liraan (*LIdar pour la Recherche Antarctique Aérosol et Nuages*, Lidar for antarctic aerosol and cloud research, in English) was first installed in 1988 and began operations in April 1989. **Liraan is part of the Network for Detection of Atmospheric Composition Changes (NDACC). It is worth mentionning that DDU and Concordia are the only lidar sites of the NDACC in Antarctica. Since 1989, DDU** system has undergone major upgrades in 1991 and 2002-2004 to include ozone measurements (later discontinued) and to improve lidar performance, with an increasing focus on aerosol detection. Details of the original configuration and previous upgrades can be found in Sacco et al. (1989); Stefanutti et al. (1991) and David et al. (2012). This paper presents the latest major update of the instrumental setup, carried out between 2022 and 2024. The main modifications include the replacement of the laser source to enable simultaneous emission at 355, 532 and 1064 nm, and the installation of a UV-dedicated polychromator incorporating polarization and Raman detection channels. The modernisation of Liraan is essential to preserve its long-term measurement record and to address evolving scientific needs in stratospheric studies.

Section 2 describes the new instrumental configuration of the DDU lidar system. Section 3 presents data preprocessing, the lidar inversion methodology, and the associated uncertainty analysis. The method for retrieving aerosol size distributions from Liraan measurements is then introduced. The results section presents a 532 nm scattering ratio time series spanning 1991-2025 at DDU, along with time series and profiles of scattering ratios at 355 nm, 532 nm and 1064 nm and depolarization ratios at 355 nm and 532 nm derived from 2025 observations. Finally, advanced retrievals linking optical properties to microphysical parameters are illustrated through two 2025 case studies.

2 Instrumental set-up

Initially designed for winter campaigns during its early decades of operation, Liraan is now operated year-round at night, subject to weather conditions. Typical measurement sessions last around 1h30 with extended sessions up to 8h depending on the season and the interest of the sounded atmospheric scene. A schematic of the lidar system is shown in Figure 1, and the current section provides more details about the instrument architecture. The companion **Table 1 summarizes the main parameters of DDU system.**

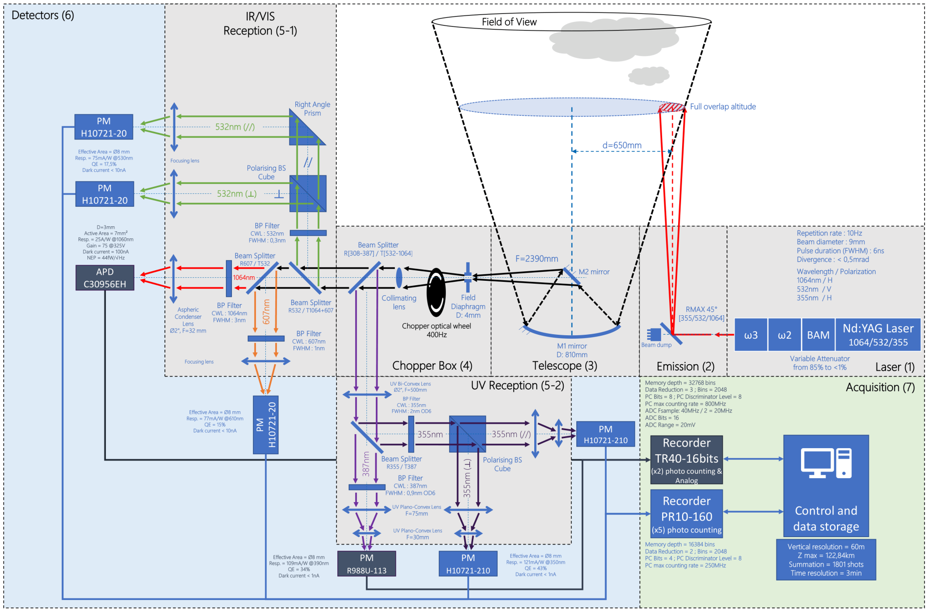

Figure 1. Detailed description of the hardware configuration and main parameters of Liraan.

2.1 Emission

Liraan is a multispectral Rayleigh-Mie lidar operating in the UV, visible and infrared spectral ranges. The source is a Nd:YAG laser (Lumibird Qsmart-850), optically pumped by a flashlamp operated at 629 V and Q-switched using external synchronisation electronics. The fundamental emission wavelength is 1064 nm, with second and third harmonics generated to produce simultaneous emission at 355, 532 and 1064 nm. The laser emits 6 ns pulses at a repetition rate of 10 Hz. The energy distribution among the three wavelengths is controlled by adjusting the temperature of the harmonic generator crystals, resulting in a total pulse energy of approximately 500 mJ. A high-reflectivity laser mirror ($R_{avg} > 98\%$), optimised for angles of incidence

Emission	
Wavelengths	355, 532, 1064 nm
Frequency	10 Hz
Beam diameter	9 mm
Pulse duration	6 ns
Divergence	< 0.5 mrad
Reception	
Telescope diameter	810 mm
Focal distance	2390 mm
Distance telescope - emission	650 mm
Acquisition	
Vertical resolution	60 m
Max. Altitude	122 km
Time resolution	3 min (1801 shots)

Table 1. Main parameters of the emission, reception and acquisition of DDU lidar system.

between 0° and 50° and covering the 350-1100 nm spectral range, redirects the laser beam toward the atmosphere at a nominal incidence angle of 45°.

2.2 Telescope

A co-located 810 nm diameter Newton telescope collects backscattered photons from atmospheric molecules and particles. A field stop diaphragm of 4 mm diameter results in a full-angle field of view of 1.7 mrad. The secondary mirror introduces an approximately 10% transmission loss due to central obscuration. Full geometrical overlap (overlap factor of 1) is achieved at an altitude of approximately 1.5 km.

2.3 Chopper

The backscattered light collected by the telescope passes through a mechanical chopper wheel located at the focal plane. The chopper blocks intense signals from low altitudes to prevent detector saturation. The chopper wheel rotates at 400 revolutions per second, corresponding to a period of 2500 μs.

An opto-Schmitt sensor detects the position of the slits and provides a high output signal when the optical path through the wheel is clear. A switching signal is then generated to synchronise the lidar system and trigger laser emission and data acquisition. The laser trigger delay is adjusted using dedicated timing electronic device. This delay defines the lidar blind zone, currently around 5km.

2.4 Reception units

On the reception end, a first dichroic mirror separates the UV from the visible and IR wavelengths, which are then guided to the two different receiver units.

The visible/IR receiver unit contains two dichroic beamsplitters. The first directs the 532 nm signal through a narrowband filter and onto a polarizing cube, which splits the beam into parallel and perpendicular polarization components ($532_{//}$ and $532_{\perp}$ respectively) with respect to the laser polarization. Both components are detected by photomultiplier tubes (PMT). The 607 nm and 1064 nm signals transmitted by the first beamsplitter are separated by a second one, filtered by narrow bandpass filters, and detected by a PMT and an avalanche photodiode (APD), respectively.

In the UV polychromator, a beamsplitter separates the 355 nm and 387 nm signals, which are then directed onto a narrowband filter. The 355 nm channel is further split into parallel and perpendicular polarization components using a polarizing cube. Each component ($355_{//}$, $355_{\perp}$, 387) is then detected by a photomultiplier.

Except for the 1064 nm channel, all detectors are Hamamatsu H10721 series PMTs, which are compact modules with integrated high-voltage power supplies. The signals from these PMTs are recorded using photon-counting (PC) channels. The 387 nm channel is detected by a different PMT (Hamamatsu R9880U), operated at high-voltage and recorded in both photo-counting and analog modes. The 1064 nm signal is detected by an APD (Excelitas E39056EH series) cooled using a thermo-electric cooler (TEC). The TEC can lower the APD temperature down to 0°C to improve its sensitivity in the infrared range. The APD signal is sampled simultaneously by a 16-bit analog-to-digital converter (ADC) and a photon-counting recorder. These two acquisition modes are combined to extend the dynamic range of the lidar: when strong signals from low-altitude clouds exceed the photon-counting saturation limit, they can still be accurately recorded using the analog channel.

All signals are time resolved with a sampling interval of 400 ns, corresponding to a range resolution of 60 m. A total of 2048 bins are recorded, corresponding to a maximum altitude of 122.8 km. Signals are integrated over 1801 laser shots (3 min) before being stored.

Access to the instrument for maintenance is highly constrained and requires careful planning, therefore upgrades are a continuous process. This article presents the main recent upgrades of Liraan, as well as those planned for the upcoming field campaigns. A dedicated power supply for the PMTs of the low-intensity channels was installed in early 2026 and will increase the signal to noise ratio (SNR) of polarization and Raman channels, while also allowing higher emitted energy without causing the saturation of high-intensity channels. A motorised mirror mount for the emission mirror is planned for installation in 2027 and is expected to improve the transmitter-receiver alignment.

3 Data processing

This section introduces the data processing steps used to retrieve optical properties from raw lidar measurements, along with the associated uncertainty assessment. **These algorithms have been developed by the authors specifically for Liraan system.** The relevant parameters are the backscatter ratios at 355, 532 and 1064 nm, denoted R_{355}, R_{532} and R_{1064} respectively, and the aerosol depolarization ratios at 355 and 532 nm, denoted $\delta_{355,\mathrm{aer}}$ and $\delta_{532,\mathrm{aer}}$ respectively. Here we define the backscatter ratio as the ratio of the total backscatter coefficient ($\beta_{\lambda,\mathrm{aer}}$) to the molecular backscatter coefficient ($\beta_{\lambda,\mathrm{mol}}$, see equation 1). The depolarization ratio is defined as the linear particle depolarization ratio, i.e., the ratio of the perpendicular to the parallel particle backscatter coefficients ($\beta_{\lambda,\mathrm{aer},\perp}$ and $\beta_{\lambda,\mathrm{aer},//}$, see equation 2).

$$R_\lambda = \frac{\beta_{\lambda,aer} + \beta_{\lambda,mol}}{\beta_{\lambda,mol}} \tag{1}$$

$$\delta_{\lambda,aer} = \frac{\beta_{\lambda,aer,\perp}}{\beta_{\lambda,aer,//}} \tag{2}$$

3.1 Pre-processing steps

Lidar measurements acquired at DDU are primarily processed using a Klett inversion algorithm. Although Raman channels at 387 nm and 607 nm are available, their use is limited to specific cases with high enough SNR. Hardware upgrades are planned for future field campaigns to improve the SNR of Raman channels.

Raw measurements are acquired as 3-minute files and subsequently integrated over 15-minute intervals, which are appropriate for stratospheric dynamics. Longer integrations of 90-minute are also performed to improve the SNR and reduce the uncertainties associated with the retrieved optical parameters. The integrated signals are then corrected for background sky noise by subtracting the mean signal at high altitudes, typically between 60 and 120 km.

As shown in Figure 1, 355 nm and 532 nm measurements are each acquired with co-polarized and cross-polarized channels, which are recombined to obtain the total signal. This recombination requires gain calibration between both channels, involving the selection of an aerosol-free reference altitude z_0 and the use of molecular depolarization factors at 355 and 532 nm. The interference filters used for the 355 nm and 532 nm channels have full widths at half maximum (FWHM) of 2 nm and 1 nm, respectively. The corresponding molecular depolarization factors are $\delta_{\mathrm{mol},355} = 10{,}86 \times 10^{-3}$ and $\delta_{\mathrm{mol},532} = 4{,}24 \times 10^{-3}$ (Kong et al., 2023). The total lidar signal at wavelength λ can be written as follows:

$$P_{\lambda,T} = P_{\lambda,//} + K P_{\lambda,\perp} \tag{3}$$

Where the gain K is computed in aerosol-free region z_0:

$$K = \delta_{mol,\lambda} \frac{P_{\lambda,//}(z_0)}{P_{\lambda,\perp}(z_0)} \tag{4}$$

Cross-polarized channels are corrected for crosstalk using equation 5. The measured signals in the parallel and perpendicular channels are denoted $\mathrm{P}_{\lambda,//,\mathrm{m}}$ and $\mathrm{P}_{\lambda,\perp,\mathrm{m}}$, respectively. Pollution from the perpendicular to the parallel channel can be reasonably considered negligible, so that $\mathrm{P}_{\lambda,//} = \mathrm{P}_{\lambda,//,\mathrm{m}}$. Conversely, pollution from the parallel to the perpendicular channel, denoted δ_{C} is not negligible and depends on both the optical alignment and the specifications of the polarization beam-splitter cubes. This parameter can be estimated using an aerosol-free reference altitude, z_0, and the molecular depolarization ratio. The corrected perpendicular signal can be expressed as follows:

$$P_{\lambda,\perp} = \frac{P_{\lambda,\perp,m} - \delta_C P_{\lambda,//}}{1-\delta_C} \tag{5}$$

Where the crosstalk correction parameter δ_C is computed as follows:

$$\delta_C = \frac{\frac{P_{\lambda,\perp,m}(z_0)}{P_{\lambda,//}(z_0)} - \delta_{mol}}{1-\delta_{mol}} \tag{6}$$

Since this correction method is based on measured signals, the results may vary slightly depending on the year, season, instrumental conditions and overall SNR. The choice of the aerosol-free region needed used in the calibration also contributes to this variability. For both the 355 nm and 532 nm channels, the estimated δ_C values are on the order of 10^{-4} to 10^{-5}, and can therefore be considered negligible.

A saturation correction is generally not required for Liraan measurements, as saturation effects are prevented at the emission stage. However, in some cases such as increased emitted energy, a lower chopper cutoff altitude, or the presence of strong tropospheric clouds, a desaturation procedure may be applied. In this approach, a correction factor ϵ (see equation 7) is optimised to restore the signal profile. This factor is determined so that the corrected signal matches the expected Rayleigh signal in an aerosol-free region of strong signal, typically in the upper troposphere.

$$P_\lambda = \frac{P_{\lambda,m}}{1-\epsilon P_{\lambda,m}} \tag{7}$$

The optimisation results in ϵ values that tend toward 0 for most measurements, and reach values on the order of 1×10^{-2} to 2×10^{-2} when significant saturation is observed.

Multiple scattering effects are neglected in Liraan measurements processing. This assumption is valid for the optically thin stratospheric aerosol and cloud layers commonly observed at DDU, but may induce biases under conditions of dense PSC presence.

Finally, ozone absorption along the lidar path must be accounted for. Ozone extinction is significant at 532 nm within the Chappuis band. It is also considered at 355 nm, located between the Hartley and Chappuis bands, while it is neglected at 1064 nm (Serdyuchenko et al., 2014, Fig. 2). Ozone absorption cross-sections at 355 nm and 532 nm are taken from Serdyuchenko et al. (2014). At 355 nm, the temperature dependence of the cross-section is considered for temperature ranging from 193 K and 293 K. Daily ozone concentration profiles above DDU are obtained from the Microwave Limb Sounder (MLS) satellite instrument. The correction is applied to the lidar signal P_λ through a transmission factor $C_{O_3,\lambda}$ defined as:

$$C_{O_3,\lambda} = e^{2\,\tau_{O_3,\lambda}} \tag{8}$$

with

$$\tau_{O_3,\lambda}(z) = \int_0^z \sigma_{O_3,\lambda}(z')n_{O_3}(z')dz' \tag{9}$$

where $\sigma_{O_3,\lambda}$ is the ozone absorption cross-section at wavelength λ, and n_{O_3} is the ozone number density.

The lidar signal corrected from ozone absorption is obtained by multiplying the lidar signal by the transmission factor $C_{O_3,\lambda}$.

The parallel and perpendicular lidar signals, corrected from background sky noise, calibrated to be recombined in a total lidar signal, corrected from cross-talk, potential saturation and ozone absorption is then used as the main input to the lidar inversion procedure described in the next section.

3.2 Lidar inversion

Once the pre-processing steps are completed, a Klett-Fernald inversion algorithm is applied, following the numerical formalism described in Fernald (1984). The main limitation of this method lies in the assumption of the lidar ratio LR, defined as the ratio of the extinction to the backscatter coefficient ($\mathrm{LR} = \frac{\alpha}{\beta}$, in sr). Although the lidar ratio can be estimated based on temperature and altitude, and thus on the type of clouds or aerosols (Chen and Chiang, 2002; Winker et al., 2009), it remains a strong assumption. The method also relies on a reference altitude at which the extinction and backscatter coefficients are known, typically chosen in an aerosol-free region where molecular properties are computed from local temperature and pressure profiles (Nicolet et al., 1982). Temperature and pressure profiles are obtained from daily radiosonde launched at DDU (operated by Météo-France) and extended above the burst altitude using ERA5 hourly profiles interpolated to the DDU location.

An iterative procedure is implemented to reduce sensitivity to the assumed values of LR and z_{ref}. Each lidar profile is evaluated over a wide range of lidar ratios LR and reference altitudes z_{ref}. The resulting backscatter ratio profiles are then compared using two independent criteria presented hereafter, and the optimal set of (LR, z_{ref}) values is retained. The tested LR values span a realistic range for stratospheric clouds and aerosols, from 10 to 140 sr (Reichardt et al., 2004; Korshunov and Zubachev, 2013; Haarig et al., 2018, e.g.,). Reference altitudes z_{ref} are selected between 20 and 30 km, excluding regions identified as aerosol or cloud layers. The inversion quality is evaluated based on the following two criteria:

- Deviation of R_λ from unity: regions outside identified aerosol or cloud layers are expected to exhibit a backscatter ratio $R_\lambda = 1$. For these altitudes, denoted $\mathrm{z_{nc}}$, a score is computed as $\sum_{\mathrm{z_{nc}}} |\mathrm{R}_\lambda - 1|$.

- Consistency of R_λ across scattering layers: if the extinction of a scattering layer is correctly accounted for in the inversion, R_λ values above and below the layer should be similar. For identified layers, the difference between these values is computed as a second score.

The first criterion is used to optimise z_{ref}, while the second is used to constrain LR. The joint minimization of both scores yields the final (LR, z_{ref}) values for the inversion of each lidar profile. This approach is particularly relevant for extended lidar scenes, as it results in a more robust and homogeneous inversion. However, given the typically low SNR of stratospheric signals and the diversity of atmospheric conditions, automated procedures should be considered with caution. In some cases, the algorithm may converge toward values that compensate for other sources of bias, such as errors in layer detection, signal saturation, minor lidar misalignment, or very low SNR. This behavior highlights the importance of robust signal preprocessing, as described in section 3.1. When the optimisation fails or yields unrealistic results, the (LR, z_{ref}) values can be overridden through manual input.

Once the scattering ratio is obtained, the linear aerosol depolarization ratio δ_{aer} is computed using equation 10, from the molecular depolarization δ_m, the backscatter ratio R, and the volume depolarization δ_v. To avoid ambiguity as the literature may feature other definitions, the linear aerosol depolarization ratio is defined here as the ratio of the perpendicular to the parallel aerosol backscatter coefficients. The volume depolarization ratio is defined as the ratio of the gain-corrected perpendicular signal to the parallel signal.

$$\delta_{aer} = \frac{R\delta_v\delta_m - \delta_m(\delta_v + 1)}{R(1+\delta_m) - (\delta_v + 1)} \quad (10)$$

3.3 Error estimation

Uncertainties in optical properties derived from lidar measurements are notoriously difficult to assess, due to the combination of multiple sources arising from both instrumental and methodological aspects of the inversion. In this paper, we consider these main sources of uncertainties, listed below in order of decreasing significance:

- Instrumental and statistical noise: all sources of uncertainty affecting the raw lidar signal measurements;
- Inversion parameters and assumptions;
- Atmospheric parameters: temperature and pressure profiles.

For PMTs allocated channels, instrumental and statistical uncertainties are primarily driven by photon-counting noise following Poisson statistics, leading to a rapid degradation of the SNR with altitude. At high altitudes, particularly in the stratosphere, the low number of detected photons results in large relative uncertainties, which can be further amplified by the inversion procedure. The standard deviation $\sigma_{\mathrm{S}}(\mathrm{z})$ of the signal $S(z)$ is therefore given by the quadratic sum of the Poisson uncertainty and electronic noise, and can be expressed as follows, where σ_{elec} is the standard deviation of the signal in high-altitude regions used to estimate the mean background:

$$\sigma_S^2(z) = S(z) + \sigma_{elec}^2 \quad (11)$$

For the APD allocated 1064 nm channel, an analog detection channel is used, which does not follow Poisson statistics. The standard deviation of the 1064 nm analog signal is estimated empirically and modeled as a linear function of the mean signal according to:

$$\sigma^2_{S_{1064}}(z) = A \times \overline{S_{1064}(z)} + B_0 \tag{12}$$

where $\overline{\mathrm{S_{1064}(z)}}$ is the mean 1064 nm signal at a given altitude. The coefficient A represents the multiplicative noise term associated with statistical fluctuations of the detected carriers and the effective gain of the detection chain, and is therefore expected to be independent of altitude and atmospheric conditions. The additive term $\mathrm{B_0}$ accounts for signal-independent noise contributions, including electronic noise and digitization effects, and is estimated from the temporal variance of the background signal measured in an altitude region free of atmospheric returns. Both parameters are derived from a global fit over a broad range of altitudes, excluding saturated and cloudy regions, and are assumed to be constant for a given instrumental configuration and integration time.

For each channel, the standard deviation is propagated through the pre-processing steps described in the previous section, including integration, background, crosstalk and saturation corrections. A Monte-Carlo method is then implemented: 200 signals are simulated according to $\mathrm{S_i(z) = S(z) + \epsilon_i(z)}$ where $\mathrm{\epsilon_i(z)} \sim \mathcal{N}(0, \sigma^2_{\mathrm{S}})$. Each of these signals is individually inverted, resulting in a set of 200 backscatter ratio profiles ($\mathrm{R_{range,stat}}$). The statistical uncertainty is then estimated as

$$\sigma_{R,stat}(z) = \sigma(R_{range,stat})(z) \tag{13}$$

The uncertainty in the backscatter ratio associated with the Klett inversion parameters is mainly driven by the choice of the lidar ratio values assigned to the identified scattering layers and the clear-sky reference altitude. A similar method is applied to both parameters. Starting from the optimised value $\mathrm{LR_{opti}}$ obtained as described in the previous section, additional inversions are computed by varying the lidar ratio within the range $[\mathrm{LR_{opti}} - 20; \mathrm{LR_{opti}} + 20]$ while keeping all other parameters fixed. This results in a set of backscatter ratio profiles ($\mathrm{R_{range,LR}}$) and the associated uncertainty is defined as

$$\Delta_{R,LR}(z) = \frac{1}{2}\left|\max(R_{range,LR}) - \min(R_{range,LR})\right| \tag{14}$$

Similarly, for $\mathrm{z_{ref}}$, inversions are computed for reference altitudes within the range $[\mathrm{z_{ref,opti}} - 1\mathrm{km}; \mathrm{z_{ref,opti}} + 1\mathrm{km}]$. The associated uncertainty is defined as

$$\Delta_{R,z_{ref}}(z) = \frac{1}{2}\left|\max(R_{range,z_{ref}}) - \min(R_{range,z_{ref}})\right| \tag{15}$$

Temperature and pressure profiles are used to compute the molecular contributions to the backscatter and extinction coefficients. To estimate the uncertainty in the backscatter ratio associated with these atmospheric parameters, a method similar to that used for LR and $\mathrm{z_{ref}}$ is applied. Inversions are performed with temperature profiles offset by $\pm 4\mathrm{K}$ and pressure profiles offset by $\pm 5\%$. The resulting uncertainty is denoted $\Delta_{\mathrm{R,atm}}(\mathrm{z})$.

The parameter ranges explored for the uncertainty estimation (±20 sr for LR, ±1 km for z_{ref}, ±4 K for temperature, and ±5% for pressure) were chosen empirically to reflect realistic variability in each parameter.

Finally, error sources are considered independent and the total error on R is written as follows:

$$\sigma_R = \sqrt{\sigma^2_{R,stat} + \Delta^2_{R_{LR}} + \Delta^2_{R_{z_{ref}}} + \Delta^2_{R_{atm}}} \tag{16}$$

In this paper, the depolarization ratio refers to $\delta_{\mathrm{aer}} = \frac{\beta_{\mathrm{aer},\perp}}{\beta_{\mathrm{aer},//}}$ and is therefore only properly defined in the presence of aerosol or clouds, as $\beta_{\mathrm{aer},//}$ tends to 0 under molecular conditions. Moreover, in presence of dense aerosol layers or clouds, $\beta_{\mathrm{aer},//} >> \beta_{\mathrm{mol},//}$ and $\beta_{\mathrm{aer},\perp} >> \beta_{\mathrm{mol},\perp}$, so that, $\delta_{\mathrm{aer}} = \frac{\beta_{\mathrm{aer},\perp}}{\beta_{\mathrm{aer},//}} \approx \frac{\beta_{\mathrm{aer},\perp}+\beta_{\mathrm{mol},\perp}}{\beta_{\mathrm{aer},//}+\beta_{\mathrm{mol},//}} = \delta_{\mathrm{vol}}$. The uncertainty in δ_{aer} is therefore estimated by propagating the uncertainty of the ratio $\frac{\mathrm{P}_\perp}{\mathrm{P}_{//}}$ and can be expressed as follows:

$$\frac{\sigma_{\delta_{aer}}}{\delta_{aer}} = \sqrt{\left(\frac{\sigma_{P_\perp}}{P_\perp}\right)^2 + \left(\frac{\sigma_{P_{//}}}{P_{//}}\right)^2} \tag{17}$$

The previous assumption is not valid for thin aerosol layers. In such cases, the propagation of uncertainties in equation 2 can be approximated as

$$\sigma_{\delta_{aer}} = \sigma_{\delta_{vol}} \frac{R_\lambda}{R_\lambda - 1} \tag{18}$$

where $\sigma_{\delta_{vol}}$ is the uncertainty on the volume depolarization ratio as expressed in equation 17.

Figure 2 shows the distribution of the uncertainties (in %) associated with scattering ratios at 355 nm (a, $\Delta_{\mathrm{R}_{355}}$), 532 nm (b, $\Delta_{\mathrm{R}_{532}}$), and 1064 nm (c, $\Delta_{\mathrm{R}_{1064}}$), as well as depolarization ratios at 355 nm (d, $\Delta_{\delta_{\mathrm{aer},355}}$) and 532 nm (e, $\Delta_{\delta_{\mathrm{aer},532}}$), derived from all DDU measurements acquired between April 2024 to October 2025. This figure shows that scattering ratio uncertainties span a wide range of values. They are primarily driven by altitude and the magnitude of scattering ratio, and exhibit similar patterns across all wavelengths. Uncertainties are generally higher at 355 nm than at 532 nm. The infrared channel exhibits higher R values; although the overall pattern remains similar, a larger variability is observed for strong signals.

Depolarization ratio uncertainties also mostly depend on δ_{aer} values and altitude. Scattering layers with significant depolarization typically display uncertainties between 10% and 70%. The uncertainty $\Delta_{\delta_{\mathrm{aer}}}$ increases rapidly with altitude above 17,5 km, as the SNR of the perpendicular channels decreases.

4 Particle size distribution estimation

Combining optical properties at different wavelengths is commonly used for particle classification and microphysical retrievals. Using a multi-wavelength (UV - visible - IR) lidar configuration, particle size distributions can be retrieved from a set of observables under appropriate assumptions. The methodology applied in this study has been described in detail in Jumelet et al. (2008) and applied to liquid PSC particles observed in the Arctic in Jumelet et al. (2009). As a short summary, the retrieval of a lognormal particle size distribution, characterized by three parameters (total number concentration in cm^{-3}, mode radius in μm and geometric standard deviation) relies on 6 input variables: aerosol backscatter coefficients at 3 wavelengths (UV, visible and IR) and their associated uncertainties, estimated following the approach described in section 3.3. A two-step procedure is considered.

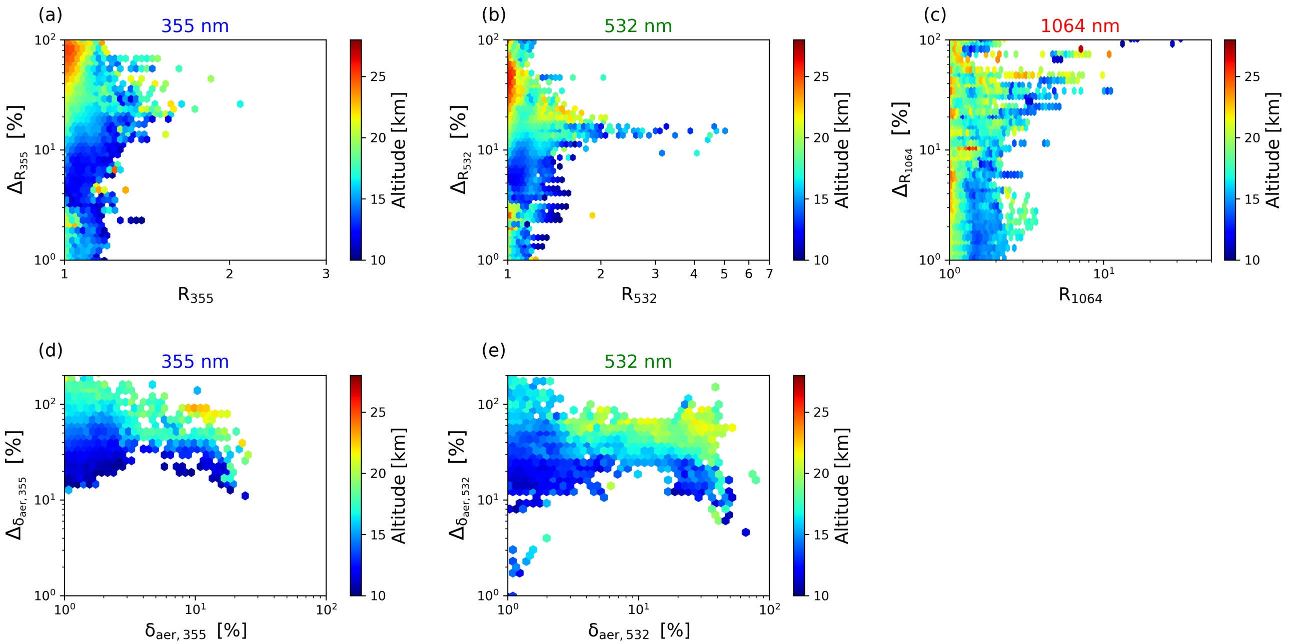

Figure 2. Distribution of estimated errors, in percentage, associated with scattering ratios at 355 nm (a, $\Delta_{\mathrm{R}_{355}}$), 532 nm (b, $\Delta_{\mathrm{R}_{532}}$), 1064 nm (c, $\Delta_{\mathrm{R}_{1064}}$), depolarization ratios at 355 nm (d, $\Delta_{\delta_{\mathrm{aer},355}}$) and 532 nm (e, $\Delta_{\delta_{\mathrm{aer},532}}$) derived from all measurements from April 2024 to October 2025. The (x, y) space is discretized into hexagonal bins and the color of each bin represents the mean altitude of the samples within the bin. Bins containing fewer than five points are omitted

First, a box model computes the equilibrium chemical composition under given environmental conditions (pressure, temperature, total HNO_3, total H_2O volume mixing ratios) for a wide range of particle size distributions. The corresponding refractive index is then derived. In this study, only liquid particles are considered (depolarization below 5% and stratospheric temperature above 195 K) allowing the use of Mie theory to compute the backscatter coefficients associated with each distribution.

Second, these solutions are compared with DDU measurements to identify the best match. A cost function is computed and minimized over the look-up table to define a cluster of possible solutions, that is filtered around 1 sigma of the median before identification of the cost function minimum. This filter mitigates the high non-linearity of the optical model, aiming at the most probable solution. Accurate uncertainty estimates are critical in this approach.

A unimodal size distribution is assumed here, although the methodology can handle multimodal distributions provided that one mode is prescribed. This assumption is generally valid at the latitude of DDU outside major recent volcanic eruption events, as stratospheric particles observed above the station typically result from long-range transport from mid-latitudes. During transport, larger particle modes are efficiently removed by sedimentation within days to weeks, while relatively stable temperature conditions above DDU support the assumption of quasi-steady microphysical processes. Examples of applications using Liraan measurements can be found in the next section.

5 Results

In this section, we present measurements obtained with the new lidar configuration along with the reprocessing of previous measurements, as the updated processing has been applied retroactively to the entire DDU dataset. Figure 3 shows the resulting time series of backscatter ratio at 532 nm from February 1991 to October 2025 **as a function of altitude, from 8 to 28 km**. This figure highlights the unique long-term record acquired with the instrument, which, to our knowledge, remains the only continuously operated stratospheric lidar over this 35-year period in Antarctica. It also shows that the measurement frequency has significantly increased since the first decade of observations. On top of a more sustained observational schedule, a growing scientific interest in stratospheric aerosol perturbations has led to the implementation of continuous summertime operations.

Figure 3 presents the complete reprocessed lidar measurements archive, illustrating the recent increase in perturbation events in the Antarctic stratosphere, especially with the Australian 2020 wildfires (Tencé et al., 2022; Khaykin et al., 2020) and the exceptional Hunga eruption in 2022, whose impact has been extensively documented (Khaykin et al., 2022; Millán et al., 2022; Kloss et al., 2022; Zhu et al., 2025). Liraan sampled the Hunga stratospheric aerosol plume for approximately two years, providing an extensive observational record of a single stratospheric event from a ground-based site. The present article does not include further analysis on the Hunga event, as it will be the subject of a dedicated study.

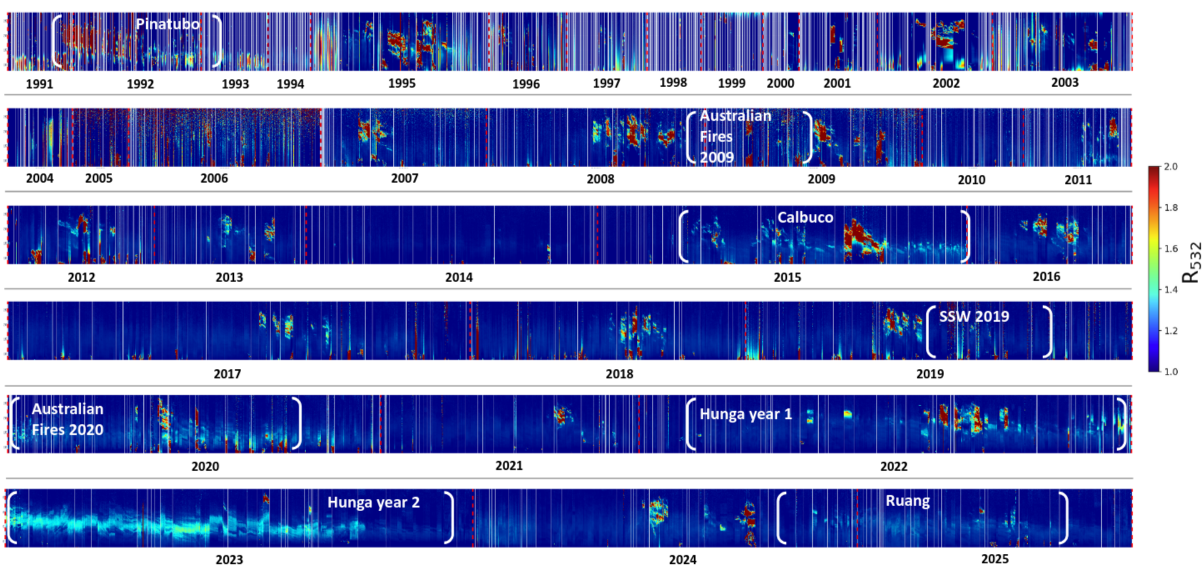

Figure 3. Time series of 532 nm backscatter ratio acquired at DDU between February 1991 and October 2025**, as a function of altitude from 8 to 28 km.** The time scale is not linear and depends on the number of available measurements. Each individual profile is integrated over 15 minutes. Dashed red vertical lines delimit the different years. White vertical bands indicate periods where at least one day separates two consecutive measurements. White brackets and labels highlight significant stratospheric perturbations.

Figure 4 shows a PSC measurement obtained at DDU on the 9th of July, 2025. The UV, visible and infrared channels exhibit a consistent dynamic over the stratospheric range, and the layer extending from 19 to 21.3 km display scattering

properties of a PSC. At 20 km, R_{355}, R_{532} and R_{1064} peak at 1.4, 1.86 and 6.2, respectively, while $\delta_{\mathrm{aer},355}$ and $\delta_{\mathrm{aer},532}$ peak at 3.6 % and 13.3 % respectively.

Figure 4 is a clear example of a nitric acid trihydrate (NAT) PSC detection: the non-zero depolarization ratio values indicate that the observed cloud cannot be a supercooled ternary solution (STS), which would only contain liquid droplets. The temperature at 20 km is approximately 5 K above the $\mathrm{T}_{\mathrm{ICE}}$ threshold. An ice PSC would also be expected to display significantly higher scattering ratio values (Achtert and Tesche, 2014; Pitts et al., 2018). $\mathrm{T}_{\mathrm{NAT}}$, $\mathrm{T}_{\mathrm{STS}}$ and $\mathrm{T}_{\mathrm{ICE}}$ formation threshold temperatures have been calculated with H_2O concentration of 4.3 ppm and HNO_3 concentration of 8.6 ppb taken from MLS measurements above DDU on the 9th of July, 2025 (Tencé et al., 2023).

This example did not need the multi-wavelength capacity of the lidar to determine the detected PSC type. However, the 355 nm and 1064 nm channels could help resolve less obvious PSC observations, as Reichardt et al. (2004) suggest. Building a PSC classification based on multi-wavelength optical parameters retrieved from DDU lidar measurements is one of the objective of this new instrumental configuration.

Figure 5 presents the 2025 time series of Liraan measurements at DDU for the five variables introduced previously: R_{355}, R_{532}, R_{1064}, $\delta_{\mathrm{aer},355}$ and $\delta_{\mathrm{aer},532}$. The color scales for 5 a, b and c are fixed between 1 and 2.5 to highlight differences between the UV, visible, and infrared channels, although this reduces the contrast between aerosol and background conditions at 355 nm and 532 nm. Similarly, both depolarization color scales are fixed from 0 to 10%. This time series is based on 15 min integrated measurements, enabling fine-scale observation of aerosol layers.

The 2025 polar stratosphere has been impacted by the Ruang volcanic eruption (Khaykin et al., 2026), and its aerosols are clearly detected at 355, 532, and 1064 nm since October 2024 (see Figure 3). The main plume altitude decreases in early 2025, in accordance with polar stratosphere dynamics. Ruang aerosols exhibit a stable optical signature throughout the year; no significant depolarization is observed, and scattering ratios are approximately of 1.15, 1.2 and 1.75 at 355, 532, and 1064 nm, respectively. Between mid-June and August, a few PSCs are observed with stronger optical signatures and depolarizing ice crystals.

Depolarization at 355 and 532 nm shows consistent behaviour, with background values close to zero for non-depolarizing aerosol layers up to 20 km and noisier signals above this altitude. This behaviour is expected due to low SNR conditions and the definition of the depolarization ratio itself.

Figure 6 shows backscatter ratio (Fig. 6a) and depolarization ratio (Fig. 6b) profiles for 4 April 2025 (dashed lines) and 17 August 2025 (solid lines). On both dates, depolarization values are close to zero, consistent with molecular values $\delta_{\mathrm{mol},355}$ and $\delta_{\mathrm{mol},532}$. On 4 April 2025, the aerosol layer extends from 8.5 to 21 km, with peak backscatter ratio values of 1.15, 1.22 and 1.78 at 355, 532 and 1064 nm, respectively. On 17 August 2025, the aerosol layer extends from 8 to 15.8 km, with peak backscatter ratio values of 1.1, 1.18 and 1.78 at 355, 532 and 1064 nm, respectively. These optical properties are consistent with aged volcanic sulfate aerosols, clearly standing out from background aerosol conditions.

As an illustration of the microphysical retrieval capabilities of the lidar, these scattering properties are used to apply the particle size distribution procedure described in section 4. Two look-up tables are constructed for the layers identified on the profiles shown in Fig. 6a and b, with temperature and altitude respectively set at (223.4 K , 14.1 km) and (202.2 K , 13 km).

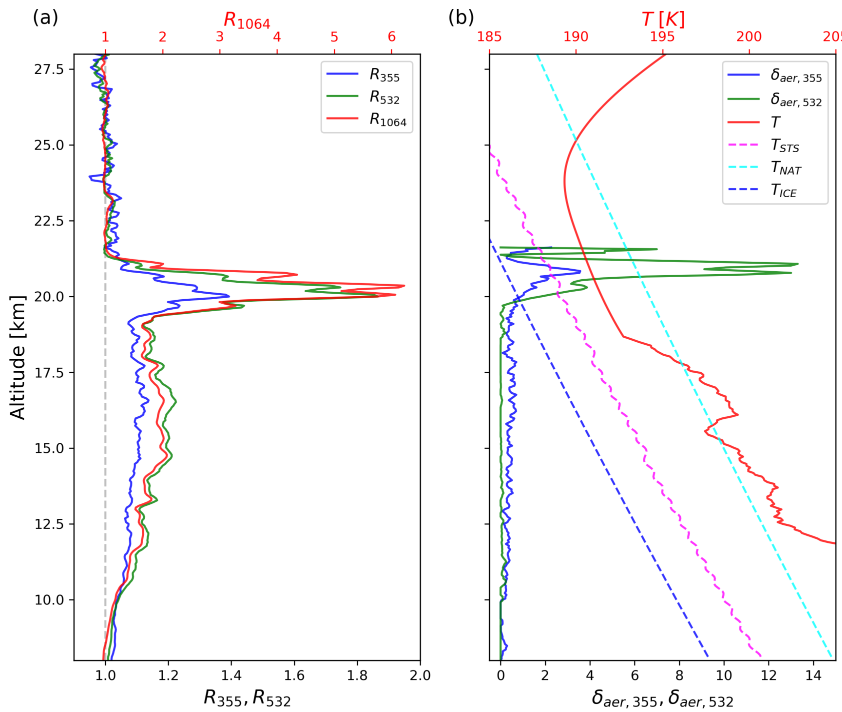

Figure 4. PSC measurement acquired at DDU on the 9th July, 2025. (a) Backscatter ratios at 355 nm (R_{355}, blue line), 532 nm (R_{532}, green line), and 1064 nm (R_{1064}, red line). (b) Depolarization ratios at 355 nm ($\delta_{\mathrm{aer,355}}$, blue line) and 532 nm ($\delta_{\mathrm{aer,532}}$, green line). Temperature profile from the local daily radiosondes launched by Météo-France, extended by ERA5 reanalysis above the burst altitude, is shown in red line. PSC formation threshold temperatures $\mathrm{T}_{\mathrm{NAT}}$, $\mathrm{T}_{\mathrm{STS}}$ and $\mathrm{T}_{\mathrm{ICE}}$ are shown in cyan, magenta and blue dashed lines, respectively.

MLS measurements above DDU indicate H_2O concentrations of 4.1 ppm on 4 April 2025 and 2.4 ppm on 17 August 2025 and HNO_3 concentrations of 2.8 ppb on 4 April 2025 and 2.3 ppb on 17 August 2025. The input parameters and results of the aerosol size distribution retrieval are summarised in Table 2.

The median radii retrieved for 4 April 2025 and 17 August 2025 are 0.3 μm and 0.24 μm, respectively, suggesting a decrease over four months of atmospheric transport. The particle concentration remains relatively stable, although slightly higher values are observed in August, consistent with the enhanced backscatter coefficients measured by the lidar. The increase in the surface area and the volume densities, respectively A and V, is expected as temperatures decrease during winter. On 17 August 2025, the temperature of 202.2 K at 14.3 km remains above the PSC formation threshold temperature $\mathrm{T}_{\mathrm{NAT}}$, confirming the aerosol nature of the observed layer.

The retrieved size distribution parameters are consistent with expected values for stratospheric aged volcanic aerosol plumes. To our knowledge, the only other microphysical estimate for the 2024 Ruang eruption was published in Dodangodage et al.

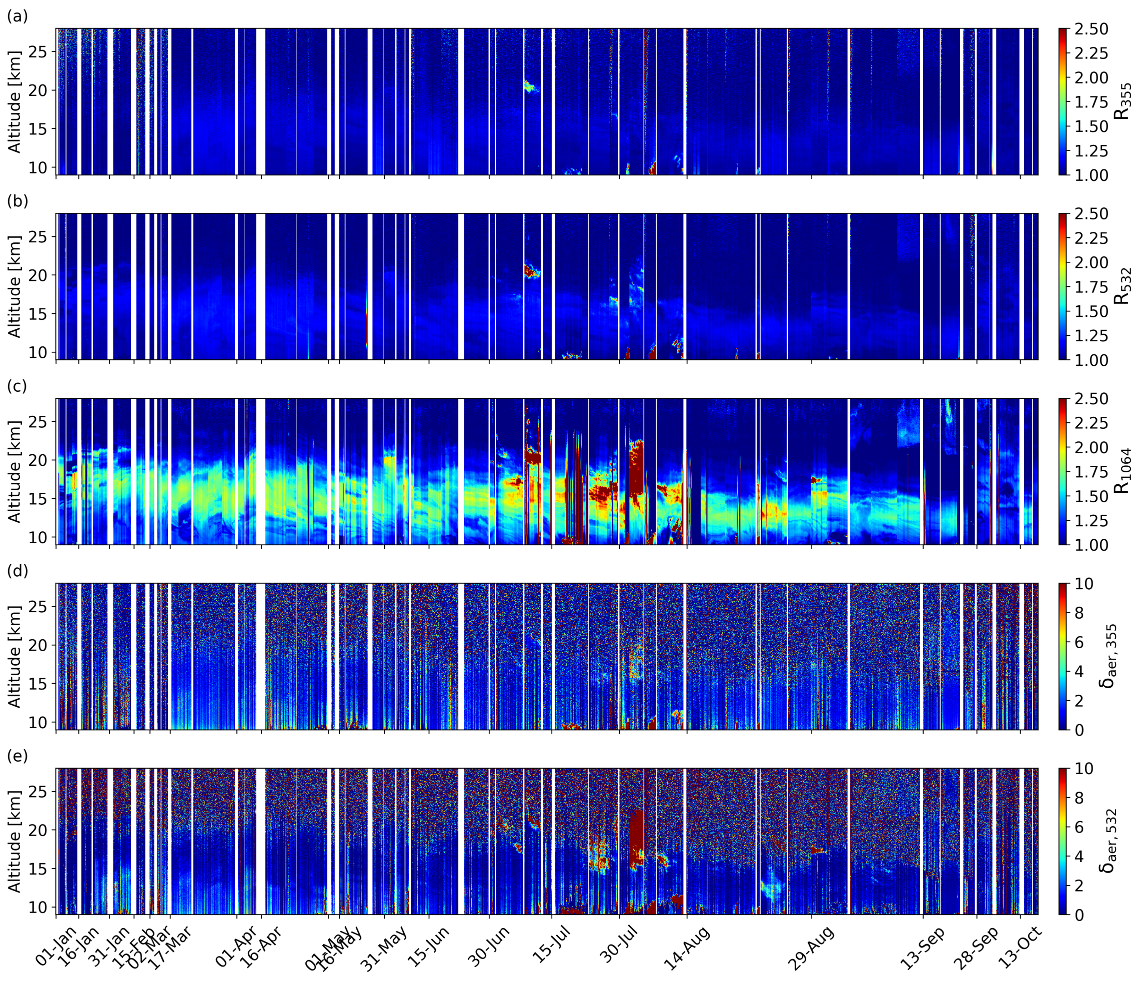

Figure 5. 2025 DDU lidar times series, from top to bottom: backscatter ratios at 355 nm (R_{355}), 532 nm (R_{532}), 1064 nm (R_{1064}), depolarization ratios at 355 nm ($\delta_{\mathrm{aer},355}$) and 532 nm ($\delta_{\mathrm{aer},532}$). The time axis is not linear and depends on the number of available measurements. Each individual profile is integrated over 15 min.

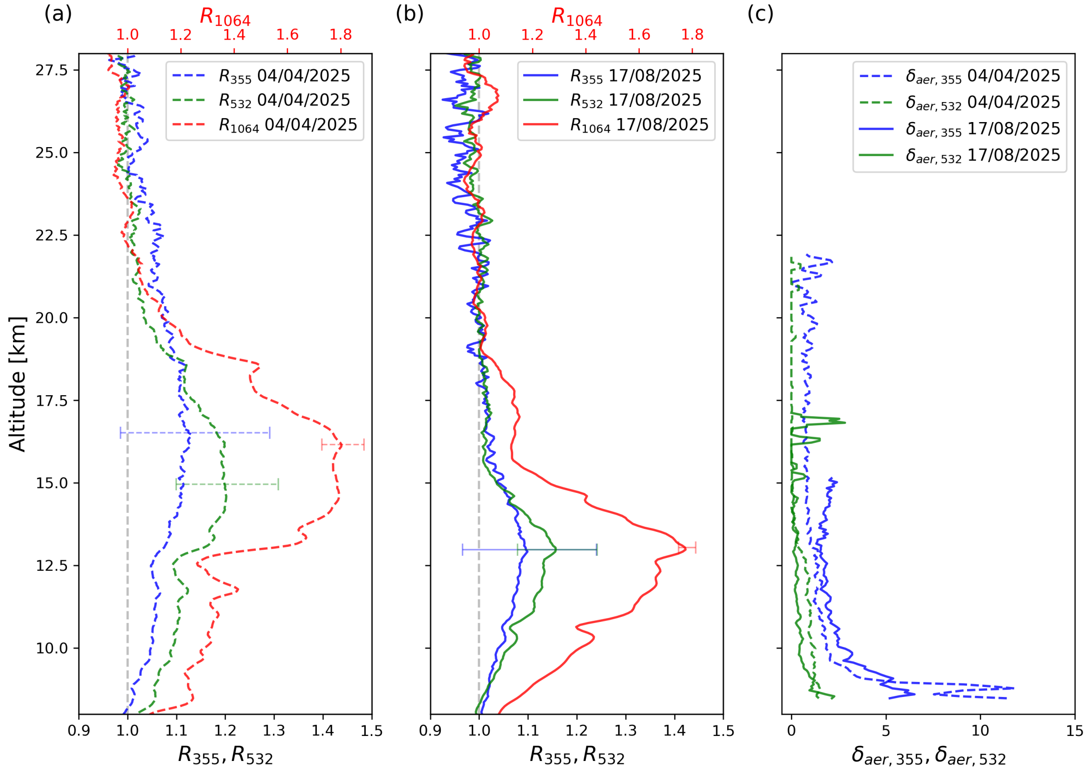

Figure 6. Backscatter ratios R_{355}, R_{532}, R_{1064} (a and b; blue, green, and red, respectively) and depolarization ratios $\delta_{\mathrm{aer},355}$ and $\delta_{\mathrm{aer},532}$ (c; blue and green, respectively) profiles acquired at DDU on 4 April 2025 (dashed lines) and 17 August 2025 (solid lines).

(2025) and reports an average median radius of 0.127 μm. This value is significantly lower than our estimations and closer to expected background stratospheric aerosol conditions. However, direct comparison between these results remains difficult, as the observations in Dodangodage et al. (2025) were performed in April and June 2024 between 0.86°S and 12.46°N, and the median radius is derived from fitting aerosol infrared transmission spectra using satellite observations from the Atmospheric Chemistry Experiment (ACE). More than one year of atmospheric transport and chemical evolution separates the two retrievals. Nevertheless, such microphysical estimates at high southern latitudes remain scarce and may provide valuable reference constraints for future studies.

6 Conclusions

The stratospheric aerosol and cloud lidar operated at the French Antarctic station Dumont d'Urville has been successfully upgraded over a series of campaigns conducted between 2022 and 2025. Improvements to the laser source, receiving optics,

Date	04/04/2025	17/08/2025
$z[km]$	14.1	13
$\beta_{355}[m^{-1}.sr^{-1}]$	$1.30.10^{-7}$	$1.59.10^{-7}$
$\Delta_{\beta_{355}}[\%]$	86	115
$\beta_{532}[m^{-1}.sr^{-1}]$	$4.86.10^{-8}$	$4.63.10^{-8}$
$\Delta_{\beta_{532}}[\%]$	46	42
$\beta_{1064}[m^{-1}.sr^{-1}]$	$1.11.10^{-8}$	$1.36.10^{-8}$
$\Delta_{\beta_{1064}}[\%]$	20	18
$T[K]$	223.4	202.2
$P[hPa]$	123.1	133.6
$\boldsymbol{N}$ $[cm^{-3}]$	2.9(0.87)	6.7(1.8)
$\boldsymbol{r}$ $[\mu m]$	0.30(0.03)	0.24(0.02)
$\boldsymbol{\sigma}$	1.16(0.07)	1.22(0.07)
$\boldsymbol{A}$ $[\mu m^2.cm^{-3}]$	3.54	5.45
$\boldsymbol{V}$ $[\mu m^3.cm^{-3}]$	0.38	0.49

Table 2. Optical, atmospheric and retrieved microphysical parameters of aerosol observed at DDU on 4 April 2025 and 17 August 2025. N, r and σ are the number concentration, median radius and geometric standard deviation of the retrieved lognormal distribution, respectively. A is the surface area density and V the volume density. The standard deviation of N, r and σ are given in parenthesis.

detectors, and acquisition system now allow the retrieval of backscatter coefficients at 355, 532 and 1604 nm along with depolarization ratios at 355 and 532 nm. The instrumental configuration and data processing are described in detail in sections 2 and 3, respectively.

In section 5, a unique 532 nm scattering ratio time series spanning 1991 - 2025 is presented for the first time (Fig. 3). This figure highlights the value of long-term ground-based lidar observations such as Liraan at DDU. Maintaining such systems over several decades is inherently challenging, particularly in Antarctica, where logistics are complex and access is limited to a restricted summer window of operation each year. Operating a lidar in Antarctica requires a rigorous organisation with the French polar institute IPEV (Paul-Emile Victor) and technical interventions typically extend over multiple campaigns. Further improvements are expected in the coming months, primarily aimed at increasing the signal-to-noise ratio of low intensity channels, such as cross-polarization and Raman channels.

Under these harsh environmental conditions, sustained effort and regular instrumental updates are required to preserve the integrity of the long-term record and the homogeneity of the time series, which is critical for climatological and trend studies (Tencé et al., 2023). In this context, Figure 3 documents the variability of PSC seasons and major stratospheric perturbations over the past three decades, but also highlights the work and dedication of all the researchers, engineers, operators and technicians who contributed to maintain this lidar since the 1990s.

The first multispectral measurements obtained with the new lidar configuration are presented as time series and vertical profiles in Figures 5 and 6, featuring stratospheric aerosol plumes associated with the recent Ruang volcanic eruption. These observations, representative of moderate volcanic perturbations, are used to demonstrate the aerosol size distribution retrieval methodology based on three simultaneously emitted wavelengths. The comprehensive set of optical and microphysical properties derived from the instrument, together with collocated ozone measurements in both profile and total column, further establishes Dumont d'Urville as a key observation site for monitoring air masses originating from lower latitudes. This three-wavelength capability opens new perspectives for the characterization of stratospheric aerosols and clouds in a region where observational coverage remains limited, while the multiple recent stratospheric perturbations featured in Figure 3 strongly call for monitoring activities.

Detailed characterisation of optical properties is used in particle classification and speciation. Additional microphysical properties can help investigate the temporal evolution of stratospheric aerosol plumes and air masses at the edge of the polar vortex. They also provide valuable links between lidar observations and other passive ground-based or spaceborne instruments, as well as modelling tools, through local validation and improved parametrizations at these latitudes.

While deriving trends in major volcanic activity with stratospheric impact remains challenging, wildfire-related perturbations are expected to become more frequent in the coming decades (Di Virgilio et al., 2019; Dowdy et al., 2019; Jones et al., 2022; Katich et al., 2023). Instruments capable of resolving speciation between sulfate carbonaceous aerosol therefore represent key assets to contribute to future studies in this field.

The limited ground-based instrumental coverage in polar regions makes spaceborne observations essential. The recent launch of EarthCARE, carrying the high spectral resolution lidar ATLID operating at 355 nm, marks a major advance in data quality and is expected to support a wide range of aerosol and cloud studies over the coming decade. Studies on the direct comparison between Liraan observations at DDU and ATLID have started and could and could help build up a strong regional inventory of optical and to some extent microphysical properties.

The new configuration deployed between 2022 and 2024 is now fully operational, still supported by IPEV both in funding and logistics. The DDU lidar is well positioned to extend this long-term dataset initiated in 1989, and to support future investigations on the polar stratosphere.

Data availability. The Dumont d'Urville lidar instrument is part of the NDACC international network and data are publicly available online at the NDACC/NOAA data archive (https://www-air.larc.nasa.gov/missions/ndacc/, last access: 12 May 2026; Jumelet, 2022), **and are updated on a yearly basis in compliancy with NDACC Lidar Working Group guidelines**. ERA5 reanalysis data are available on the Copernicus Climate Data Store at https://doi.org/10.24381/cds.bd0915c6 (Hersbach et al., 2018).

Author contributions. All authors contributed to the instrument overhaul, design or field campaigns. Specifically, FT and JJ are involved in data processing and scientific analysis. RHK, SB and JFM in charge of electronics, optics, maintenance and logistics. FT and IC acquired most of the measurements presented in this article and characterized the new lidar configuration. All authors are also involved in the article proofreading.

Competing interests. The contact author has declared that neither they nor their co-authors have any competing interests.

Acknowledgements. Operations on the Dumont d'Urville station are supported by the French Polar Institute IPEV (Institut polaire français Paul-Emile Victor), science program 209. This work was also supported within the EECLAT project (CNES-INSU). The lidar instrument is part of the NDACC international network. **The rejuvenation campaign also received strong support from the European Aerosol, Clouds and Trace Gases Research Infrastructure (ACTRIS).** Finally, the instrument is consistently supported by the Latmos laboratory in Paris, and Observatoire Versailles Saint-Quentin (OVSQ) in Guyancourt, France. The authors finally thank lidar yearly overwintering operators whose dedication has to be maintained throughout 12-month mission on the station.

References

Achtert, P. and Tesche, M.: Assessing lidar-based classification schemes for polar stratospheric clouds based on 16 years of measurements at Esrange, Sweden, Journal of Geophysical Research: Atmospheres, 119, 1386–1405, https://doi.org/https://doi.org/10.1002/2013JD020355, 2014.

Adriani, A., Deshler, T., Gobbi, G. P., Johnson, B. J., and Di Donfrancesco, G.: Polar stratospheric clouds over McMurdo, Antarctica, during the 1991 spring: Lidar and particle counter measurements, Geophysical Research Letters, 19, 1755–1758, https://doi.org/https://doi.org/10.1029/92GL01941, 1992.

Adriani, A., Massoli, P., Di Donfrancesco, G., Cairo, F., Moriconi, M. L., and Snels, M.: Climatology of polar stratospheric clouds based on lidar observations from 1993 to 2001 over McMurdo Station, Antarctica, Journal of Geophysical Research: Atmospheres, 109, https://doi.org/https://doi.org/10.1029/2004JD004800, 2004.

Bergeret, V., Bekki, S., Godin, S., and Mégie, G.: Analyse des variations saisonnières de l'ozone antarctique dans la basse stratosphère à partir des données Lidar et Sonde de Dumont d'Urville, Comptes Rendus de l'Académie des Sciences - Series IIA - Earth and Planetary Science, 326, 751–756, https://doi.org/https://doi.org/10.1016/S1251-8050(98)80239-5, 1998.

Cairo, F., Deshler, T., Di Liberto, L., Scoccione, A., and Snels, M.: A study of optical scattering modelling for mixed-phase polar stratospheric clouds, Atmospheric Measurement Techniques, 16, 419–431, https://doi.org/10.5194/amt-16-419-2023, 2023.

Chen, W.-N. and Chiang, Chih-Wei aand Nee, J.-B.: Lidar ratio and depolarization ratio for cirrus clouds., Applied optics, 41, https://doi.org/10.1364/ao.41.006470, 2002.

David, C., Bekki, S., Berdunov, N., Marchand, M., Snels, M., and Mégie, G.: Classification and scales of Antarctic polar stratospheric clouds using wavelet decomposition, Journal of Atmospheric and Solar-Terrestrial Physics, 67, 293–300, https://doi.org/https://doi.org/10.1016/j.jastp.2004.07.043, 2005.

David, C., Keckhut, P., Armetta, A., Jumelet, J., Snels, M., Marchand, M., and Bekki, S.: Radiosonde stratospheric temperatures at Dumont d'Urville (Antarctica): trends and link with polar stratospheric clouds, Atmospheric Chemistry and Physics, 10, 3813–3825, https://doi.org/10.5194/acp-10-3813-2010, 2010.

David, C., Haefele, A., Keckhut, P., Marchand, M., Jumelet, J., Leblanc, T., Cenac, C., Laqui, C., Porteneuve, J., Haeffelin, M., Courcoux, Y., Snels, M., Viterbini, M., and Quatrevalet, M.: Evaluation of stratospheric ozone, temperature, and aerosol profiles from the LOANA lidar in Antarctica, Polar Science, 6, 209 – 225, https://doi.org/https://doi.org/10.1016/j.polar.2012.07.001, 2012.

David-Beausire, C., Bekki, S., Godin-Beekmann, S., Mégie, G., and Chipperfield, M.: Polar stratospheric clouds climatology over Dumont d'Urville between 1989 and 1993 and the influence of volcanic aerosols on their formation, Journal of Geophysical Research, 1032, 22 163–22 180, https://doi.org/10.1029/98JD01692, 1998.

Di Virgilio, G., Evans, J. P., Blake, S. A. P., Armstrong, M., Dowdy, A. J., Sharples, J., and McRae, R.: Climate Change Increases the Potential for Extreme Wildfires, Geophysical Research Letters, 46, 8517–8526, https://doi.org/https://doi.org/10.1029/2019GL083699, 2019.

Dodangodage, R., Bernath, P. F., Wyatt, M., and Boone, C.: Atmospheric Chemistry Experiment (ACE) satellite observations of aerosols and SO2 emissions from the 2024 Ruang volcanic eruption, Journal of Quantitative Spectroscopy and Radiative Transfer, 333, 109 333, https://doi.org/https://doi.org/10.1016/j.jqsrt.2024.109333, 2025.

Donovan, D. P., van Zadelhoff, G.-J., and Wang, P.: The EarthCARE lidar cloud and aerosol profile processor (A-PRO): the A-AER, A-EBD, A-TC, and A-ICE products, Atmospheric Measurement Techniques, 17, 5301–5340, https://doi.org/10.5194/amt-17-5301-2024, 2024.

Dowdy, A. J., Ye, H., Pepler, A., Thatcher, M., Osbrough, S. L., Evans, J. P., Di Virgilio, G., and McCarthy, N.: Future changes in extreme weather and pyroconvection risk factors for Australian wildfires, Scientific Reports, 9, 10 073, https://doi.org/10.1038/s41598-019-46362-x, 2019.

Farman, J. C., Gardiner, B. G., and Shanklin, J. D.: Large losses of total ozone in Antarctica reveal seasonal ClOx/NOx interaction, Nature, 315, 207–210, https://doi.org/10.1038/315207a0, 1985.

Fernald, F. G.: Analysis of atmospheric lidar observations: some comments, Applied Optics, 23, 652–653, https://doi.org/10.1364/AO.23.000652, 1984.

Fiocco, G., Cacciani, M., Di Girolamo, P., Fuà, D., and Deluisi, J.: Stratospheric clouds at south pole during 1988 1. Results of lidar observations and their relationship to temperature, Journal of Geophysical Research: Atmospheres, 97, 5939–5946, https://doi.org/https://doi.org/10.1029/91JD03124, 1992.

Godin, S., Bergeret, V., Bekki, S., David, C., and Mégie, G.: Study of the interannual ozone loss and the permeability of the Antarctic polar vortex from aerosol and ozone lidar measurements in Dumont d'Urville (66.4°S, 140°E), Journal of Geophysical Research: Atmospheres, 106, 1311–1330, https://doi.org/https://doi.org/10.1029/2000JD900459, 2001.

Guzzi, D., Morandi, M., Santacesaria, V., Stefanutti, L., Agostini, P., Liley, B., and Wolf, J. P.: Four years of stratospheric aerosol measurements in the northern and southern hemispheres, Geophysical Research Letters, 26, 2199–2202, https://doi.org/https://doi.org/10.1029/1999GL900385, 1999.

Haarig, M., Ansmann, A., Baars, H., Jimenez, C., Veselovskii, I., Engelmann, R., and Althausen, D.: Depolarization and lidar ratios at 355, 532, and 1064 nm and microphysical properties of aged tropospheric and stratospheric Canadian wildfire smoke, Atmospheric Chemistry and Physics, 18, 11 847–11 861, https://doi.org/10.5194/acp-18-11847-2018, 2018.

Innis, J. L. and Klekociuk, A. R.: Planetary wave and gravity wave influence on the occurrence of polar stratospheric clouds over Davis Station, Antarctica, seen in lidar and radiosonde observations, Journal of Geophysical Research: Atmospheres, 111, https://doi.org/https://doi.org/10.1029/2006JD007629, 2006.

Iwasaka, Y.: Lidar measurement on the Antarctic stratospheric aerosol layer [II] The changes of layer height and thickness in winter, Journal of geomagnetism and geoelectricity, 38, 99–109, 1986.

Iwasaka, Y., Hirasawa, T., and Fukunishi, H.: Lidar Measurement on the Antarctic Stratospheric Aerosol Layer [I] Winter Enhancement, Journal of geomagnetism and geoelectricity, 37, 1087–1095, 1985.

Jones, M. W., Abatzoglou, J. T., Veraverbeke, S., Andela, N., Lasslop, G., Forkel, M., Smith, A. J. P., Burton, C., Betts, R. A., van der Werf, G. R., Sitch, S., Canadell, J. G., Santín, C., Kolden, C., Doerr, S. H., and Le Quéré, C.: Global and Regional Trends and Drivers of Fire Under Climate Change, Reviews of Geophysics, 60, https://doi.org/https://doi.org/10.1029/2020RG0007261, 2022.

Jumelet, J., Bekki, S., David, C., and Keckhut, P.: Statistical estimation of stratospheric particle size distribution by combining optical modelling and lidar scattering measurements, Atmospheric Chemistry and Physics, 8, 5435–5448, https://doi.org/10.5194/acp-8-5435-2008, 2008.

Jumelet, J., Bekki, S., Seifert, P., Montoux, N., Vernier, J.-P., and Pelon, J.: Microphysical modeling of a midlatitude "polar stratospheric cloud" event: Comparisons against multiwavelength ground-based and spaceborne lidar data, Journal of Geophysical Research: Atmospheres, 114, https://doi.org/https://doi.org/10.1029/2009JD011776, 2009.

Jumelet, J., Klekociuk, A. R., Alexander, S. P., Bekki, S., Hauchecorne, A., Vernier, J. P., Fromm, M., and Keckhut, P.: Detection of Aerosols in Antarctica From Long-Range Transport of the 2009 Australian Wildfires, Journal of Geophysical Research: Atmospheres, 125, e2020JD032 542, https://doi.org/https://doi.org/10.1029/2020JD032542, e2020JD032542 2020JD032542, 2020.

Katich, J. M., Apel, E. C., Bourgeois, I., Brock, C. A., Bui, T. P., Campuzano-Jost, P., Commane, R., Daube, B., Dollner, M., Fromm, M., Froyd, K. D., Hills, A. J., Hornbrook, R. S., Jimenez, J. L., Kupc, A., Lamb, K. D., McKain, K., Moore, F., Murphy, D. M., Nault, B. A., Peischl, J., Perring, A. E., Peterson, D. A., Ray, E. A., Rosenlof, K. H., Ryerson, T., Schill, G. P., Schroder, J. C., Weinzierl, B., Thompson, C., Williamson, C. J., Wofsy, S. C., Yu, P., and Schwarz, J. P.: Pyrocumulonimbus affect average stratospheric aerosol composition, Science, 379, 815–820, https://doi.org/10.1126/science.add3101, 2023.

Khaykin, S., Legras, B., Bucci, S., Sellitto, P., Isaksen, L., Tencé, F., Bekki, S., Bourassa, A., Rieger, L., Zawada, D., Jumelet, J., and Godin-Beekmann, S.: The 2019/20 Australian wildfires generated a persistent smoke-charged vortex rising up to 35 km altitude, Communications Earth & Environment, 1, 22, https://doi.org/https://doi.org/10.1038/s43247-020-00022-5, 2020.

Khaykin, S., Podglajen, A., Ploeger, F., Grooß, J.-U., Tence, F., Bekki, S., Khlopenkov, K., Bedka, K., Rieger, L., Baron, A., Godin-Beekmann, S., Legras, B., Sellitto, P., Sakai, T., Barnes, J., Uchino, O., Morino, I., Nagai, T., Wing, R., Baumgarten, G., Gerding, M., Duflot, V., Payen, G., Jumelet, J., Querel, R., Liley, B., Bourassa, A., Clouser, B., Feofilov, A., Hauchecorne, A., and Ravetta, F.: Global perturbation of stratospheric water and aerosol burden by Hunga eruption, Communications Earth & Environment, 3, 316, https://doi.org/https://doi.org/10.1038/s43247-022-00652-x, 2022.

Khaykin, S., Sicard, M., Leblanc, T., Sakai, T., Balugin, N., Berthet, G., Chevrier, S., Chouza, F., Feofilov, A., Gantois, D., Godin-Beekmann, S., Haddouche, A., Jin, Y., Morino, I., Kadygrov, N., Lecas, T., Liley, B., Querel, R., Taha, G., and Yushkov, V.: Global transport of stratospheric aerosol produced by Ruang eruption from EarthCARE ATLID, limb-viewing satellites and ground-based lidar observations, Atmospheric Chemistry and Physics, 26, 607–622, https://doi.org/10.5194/acp-26-607-2026, 2026.

Kloss, C., Sellitto, P., Renard, J.-B., Baron, A., Bègue, N., Legras, B., Berthet, G., Briaud, E., Carboni, E., Duchamp, C., Duflot, V., Jacquet, P., Marquestaut, N., Metzger, J.-M., Payen, G., Ranaivombola, M., Roberts, T., Siddans, R., and Jégou, F.: Aerosol Characterization of the Stratospheric Plume From the Volcanic Eruption at Hunga Tonga 15 January 2022, Geophysical Research Letters, 49, e2022GL099 394, https://doi.org/https://doi.org/10.1029/2022GL099394, e2022GL099394 2022GL099394, 2022.

Kong, Z., Yang, X., and Mei, L.: Theoretical and experimental investigation of the molecular depolarization ratio for broadband polarization lidar techniques, Opt. Express, 31, 24 897–24 913, https://doi.org/10.1364/OE.494950, 2023.

Korshunov, V. A. and Zubachev, D. S.: Determination of stratospheric aerosol parameters from two-wavelength lidar sensing data, Izvestiya, Atmospheric and Oceanic Physics, 49, 176–186, https://doi.org/10.1134/S0001433813020114, 2013.

Kremser, S., Thomason, L. W., von Hobe, M., Hermann, M., Deshler, T., Timmreck, C., Toohey, M., Stenke, A., Schwarz, J. P., Weigel, R., Fueglistaler, S., Prata, F. J., Vernier, J.-P., Schlager, H., Barnes, J. E., Antuña-Marrero, J.-C., Fairlie, D., Palm, M., Mahieu, E., Notholt, J., Rex, M., Bingen, C., Vanhellemont, F., Bourassa, A., Plane, J. M. C., Klocke, D., Carn, S. A., Clarisse, L., Trickl, T., Neely, R., James, A. D., Rieger, L., Wilson, J. C., and Meland, B.: Stratospheric aerosol—Observations, processes, and impact on climate, Reviews of Geophysics, 54, 278–335, https://doi.org/https://doi.org/10.1002/2015RG000511, 2016.

Martinsson, B. G., Friberg, J., Sandvik, O. S., Hermann, M., van Velthoven, P. F. J., and Zahn, A.: Formation and composition of the UTLS aerosol, npj Climate and Atmospheric Science, 2, 40, https://doi.org/10.1038/s41612-019-0097-1, 2019.

McCormick, M. P. and Trepte, C. R.: SAM II measurements of Antarctic PSC's and aerosols, Geophysical Research Letters, 13, 1276–1279, https://doi.org/https://doi.org/10.1029/GL013i012p01276, 1986.

Millán, L., Santee, M. L., Lambert, A., Livesey, N. J., Werner, F., Schwartz, M. J., Pumphrey, H. C., Manney, G. L., Wang, Y., Su, H., Wu, L., Read, W. G., and Froidevaux, L.: The Hunga Tonga-Hunga Ha'apai Hydration of the Stratosphere, Geophysical Research Letters, 49, e2022GL099 381, https://doi.org/https://doi.org/10.1029/2022GL099381, e2022GL099381 2022GL099381, 2022.

Nicolet, M., Meier, R., and Anderson, D.: Radiation fields in the troposphere and stratosphere - II. Numerical analysis, Planetary and Space Science 30, 935-983, 1982.

Pitts, M. C., Poole, L. R., and Thomason, L. W.: CALIPSO polar stratospheric cloud observations: second-generation detection algorithm and composition discrimination, Atmospheric Chemistry and Physics, 9, 7577–7589, https://doi.org/10.5194/acp-9-7577-2009, 2009.

Pitts, M. C., Poole, L. R., Dörnbrack, A., and Thomason, L. W.: The 2009–2010 Arctic polar stratospheric cloud season: a CALIPSO perspective, Atmospheric Chemistry and Physics, 11, 2161–2177, https://doi.org/10.5194/acp-11-2161-2011, 2011.

Pitts, M. C., Poole, L. R., Lambert, A., and Thomason, L. W.: An assessment of CALIOP polar stratospheric cloud composition classification, Atmospheric Chemistry and Physics, 13, 2975–2988, https://doi.org/10.5194/acp-13-2975-2013, 2013.

Pitts, M. C., Poole, L. R., and Gonzalez, R.: Polar stratospheric cloud climatology based on CALIPSO spaceborne lidar measurements from 2006 to 2017, Atmospheric Chemistry and Physics, 18, 10 881–10 913, https://doi.org/10.5194/acp-18-10881-2018, 2018.

Poole, L. R. and McCormick, M. P.: Polar stratospheric clouds and the Antarctic ozone hole, Journal of Geophysical Research: Atmospheres, 93, 8423–8430, https://doi.org/https://doi.org/10.1029/JD093iD07p08423, 1988.

Reichardt, J., Dörnbrack, A., Reichardt, S., Yang, P., and McGee, T. J.: Mountain wave PSC dynamics and microphysics from ground-based lidar measurements and meteorological modeling, Atmospheric Chemistry and Physics, 4, 1149–1165, https://doi.org/10.5194/acp-4-1149-2004, 2004.

Sacco, V., Castagnoli, F., Morandi, M., and Stefanutti, L.: Elastic backscattering lidar system for atmospheric measurements in Antarctica, Optical and quantum electronics, 21, 215–226, 1989.

Santacesaria, V., MacKenzie, A. R., and Stefanutti, L.: A climatological study of polar stratospheric clouds (1989–1997) from LIDAR measurements over Dumont d'Urville (Antarctica), Tellus B, 53, 306–321, https://doi.org/https://doi.org/10.1034/j.1600-0889.2001.01155.x, 2001.

Sepúlveda, E., Cordero, R. R., Damiani, A., Feron, S., Pizarro, J., Zamorano, F., Kivi, R., Sánchez, R., Yela, M., Jumelet, J., Godoy, A., Carrasco, J., Crespo, J. S., Seckmeyer, G., Jorquera, J. A., Carrera, J. M., Valdevenito, B., Cabrera, S., Redondas, A., and Rowe, P. M.: Evaluation of Antarctic Ozone Profiles derived from OMPS-LP by using Balloon-borne Ozonesondes, Scientific Reports, 11, 4288, https://doi.org/10.1038/s41598-021-81954-6, 2021.

Serdyuchenko, A., Gorshelev, V., Weber, M., Chehade, W., and Burrows, J. P.: High spectral resolution ozone absorption cross-sections; Part 2: Temperature dependence, Atmospheric Measurement Techniques, 7, 625–636, https://doi.org/10.5194/amt-7-625-2014, 2014.

Simpson, S., Chu, X., Liu, A., Robinson, W., Nott, G., Diettrich, J., Espy, P., and Shanklin, J.: Polar stratospheric clouds observed by a lidar at Rothera, Antarctica (67.5°S, 68.0°W), Proceedings of SPIE - The International Society for Optical Engineering, 5887, https://doi.org/10.1117/12.620399, 2005.

Snels, M., Scoccione, A., Di Liberto, L., Colao, F., Pitts, M., Poole, L., Deshler, T., Cairo, F., Cagnazzo, C., and Fierli, F.: Comparison of Antarctic polar stratospheric cloud observations by ground-based and space-borne lidar and relevance for chemistry–climate models, Atmospheric Chemistry and Physics, 19, 955–972, https://doi.org/10.5194/acp-19-955-2019, 2019.

Snels, M., Colao, F., Cairo, F., Shuli, I., Scoccione, A., De Muro, M., Pitts, M., Poole, L., and Di Liberto, L.: Quasi-coincident observations of polar stratospheric clouds by ground-based lidar and CALIOP at Concordia (Dome C, Antarctica) from 2014 to 2018, Atmospheric Chemistry and Physics, 21, 2165–2178, https://doi.org/10.5194/acp-21-2165-2021, 2021.

Solomon, S.: Stratospheric ozone depletion: A review of concepts and history, Reviews of Geophysics, 37, 275–316, https://doi.org/https://doi.org/10.1029/1999RG900008, 1999.

Solomon, S., Dube, K., Stone, K., Yu, P., Kinnison, D., Toon, O. B., Strahan, S. E., Rosenlof, K. H., Portmann, R., Davis, S., Randel, W., Bernath, P., Boone, C., Bardeen, C. G., Bourassa, A., Zawada, D., and Degenstein, D.: On the stratospheric chemistry of midlatitude wildfire smoke, Proceedings of the National Academy of Sciences, 119, e2117325 119, https://doi.org/10.1073/pnas.2117325119, 2022.

Stefanutti, L., Morandi, M., Guasta, M. D., Godin, S., Megie, G., Brechet, J., and Piquard, J.: Polar stratospheric cloud observations over the Antarctic continent at Dumont d'Urville, Journal of Geophysical Research: Atmospheres, 96, 12 975–12 987, https://doi.org/https://doi.org/10.1029/91JD00776, 1991.

Stefanutti, L., Morandi, M., Del Guasta, M., Godin, S., and David, C.: Unusual PSCs observed by LIDAR in Antarctica, Geophysical Research Letters, 22, 2377–2380, https://doi.org/https://doi.org/10.1029/95GL02085, 1995.

Tencé, F., Jumelet, J., Bouillon, M., Cugnet, D., Bekki, S., Safieddine, S., Keckhut, P., and Sarkissian, A.: 14 years of lidar measurements of polar stratospheric clouds at the French Antarctic station Dumont d'Urville, Atmospheric Chemistry and Physics, 23, 431–451, https://doi.org/10.5194/acp-23-431-2023, 2023.

Tencé, F., Jumelet, J., Bekki, S., Khaykin, S., Sarkissian, A., and Keckhut, P.: Australian Black Summer Smoke Observed by Lidar at the French Antarctic Station Dumont d'Urville, Journal of Geophysical Research: Atmospheres, 127, e2021JD035 349, https://doi.org/https://doi.org/10.1029/2021JD035349, e2021JD035349 2021JD035349, 2022.

Tritscher, I., Pitts, M. C., Poole, L. R., Alexander, S. P., Cairo, F., Chipperfield, M. P., Grooß, J.-U., Höpfner, M., Lambert, A., Luo, B., Molleker, S., Orr, A., Salawitch, R., Snels, M., Spang, R., Woiwode, W., and Peter, T.: Polar Stratospheric Clouds: Satellite Observations, Processes, and Role in Ozone Depletion, Reviews of Geophysics, 59, e2020RG000 702, https://doi.org/https://doi.org/10.1029/2020RG000702, e2020RG000702 2020RG000702, 2021.

van Zadelhoff, G.-J., Donovan, D. P., and Wang, P.: Detection of aerosol and cloud features for the EarthCARE atmospheric lidar (ATLID): the ATLID FeatureMask (A-FM) product, Atmospheric Measurement Techniques, 16, 3631–3651, https://doi.org/10.5194/amt-16-3631-2023, 2023.

Winker, D. M., Vaughan, M. A., Omar, A., Hu, Y., Powell, K. A., Liu, Z., Hunt, W. H., and Young, S. A.: Overview of the CALIPSO Mission and CALIOP Data Processing Algorithms, Journal of Atmospheric and Oceanic Technology, 26, 2310 – 2323, https://doi.org/10.1175/2009JTECHA1281.1, 2009.

WMO: Scientific Assessment of Ozone Depletion: 2022, GAW Report No. 278, p. 509p, 2022.

Zhu, Y., Mann, G., Newman, P. A., and Randel, W.: The Hunga Volcanic Eruption Atmospheric Impacts Report, 11, 346, https://doi.org/10.34734/FZJ-2025-05237, 2025.